A HYBRID COSMOLOGICAL HYDRODYNAMIC/N-BODY CODE BASED ON A WEIGHTED ESSENTIALLY NONOSCILLATORY SCHEME

LONG-LONG FENG,[1,2,3] CHI-WANG SHU,[4] AND MENGPING ZHANG[5]

ABSTRACT

We present a newly developed cosmological hydrodynamics code based on weighted essentially nonoscillatory (WENO) schemes for hyperbolic conservation laws. WENO is a higher order accurate finite difference scheme designed for problems with piecewise smooth solutions containing discontinuities and has been successfully applied for problems involving both shocks and complicated smooth solution structures. We couple hydrodynamics based on the WENO scheme with the standard Poisson solver–particle-mesh (PM) algorithm for evolving the self-gravitating system. The third-order low-storage total variation diminishing (TVD) Runge-Kutta scheme has been used for the time integration of the system. To test the accuracy and convergence rate of the code, we subject it to a number of typical tests, including the Sod shock tube in multiple dimensions, the Sedov blast wave, and formation of the Zel'dovich pancake. These tests validate the WENO hydrodynamics with a fast convergence rate and high accuracy. We also evolve a low-density flat cosmological model (ΛCDM) to explore the validity of the code in practical simulations.

Subject headings: cosmology: theory — large-scale structure of universe

1. INTRODUCTION

Although the universe seems to be dominated by the dark sides of both matter and energy (Turner 2002), the observed luminous universe has been existing in the form of baryonic matter, whose mass density, constrained by the primordial nucleosynthesis (Walker et al. 1991), only occupies a small amount of the total density. To account for the observational features revealed by the baryonic matter, i.e., X-ray–emitting gas in galaxies and clusters (Mulchaey 2000), intergalactic medium inferred from the Lyα forest (Rauch 1998), X-ray background radiation (Giacconi et al. 1962), the distorted spectrum of the cosmic background radiation due to the Sunyaev-Zel'dovich effect (Zel'dovich & Sunyaev 1969; Ostriker & Vishniac 1986), etc., it would be necessary to incorporate hydrodynamics into cosmological investigations. This motivation has stimulated great efforts to apply a variety of gasdynamic algorithms to cosmological simulations. For a general review of the most current work on this topic, we refer to Bertschinger (1998).

As a result of the high nonlinearity of gravitational clustering in the universe, there are two significant features emerging in cosmological hydrodynamic flow, which pose more challenges than the typical hydrodynamic simulation without self-gravity. One significant feature is the extremely supersonic motion around the density peaks developed by gravitational instability, which leads to strong shock discontinuities within complex smooth structures. Another feature is the appearance of an enormous dynamic range in space and time, as well as in the related gas quantities. For instance, the hierarchical

structures in the galaxy distribution span a wide range of length scales, from the few kiloparsecs resolved by an individual galaxy to the several tens of megaparsecs characterizing the largest coherent scale in the universe.

A variety of numerical schemes for solving the coupled system of collisional baryonic matter and collisionless dark matter have been developed in the past decades. They fall into two categories: particle methods and grid-based methods.

The particle methods include variants of the smoothed particle hydrodynamics (SPH; Gingold & Monaghan 1977; Lucy 1977) such as those of Evrard (1988), Hernquist & Katz (1989), Navarro & White (1993), Couchman et al. (1995; Hydra), Steinmetz (1996), Owen et al. (1998), and Springel et al. (2001; Gadget). The SPH method solves the Lagrangian form of the Euler equations and could achieve good spatial resolutions in high-density regions, but it works poorly in low-density regions. It also suffers from degraded resolution in shocked regions due to the introduction of sizable artificial viscosity.

The grid-based methods are to solve the Euler equations on structured or unstructured grids. The early attempt was made by Cen (1992) using a central difference scheme. It uses artificial viscosity to handle shocks and has first-order accuracy. The modern approaches implemented for high-resolution shock capturing are usually based on the Godunov algorithm. The two typical examples are the total variation diminishing (TVD) scheme (Harten 1983) and the piecewise parabolic method (PPM; Colella & Woodward 1984). Both schemes start from the integral form of conservation laws of Euler equations and compute the flux vector based on cell averages (finite volume scheme). The TVD scheme modifies the flux using an approximate solution of the Riemann problem with corrections added to ensure that there are no postshock oscillations. While in the PPM scheme, the Riemann problem is solved accurately using a quadratic interpolation of the cell-average densities that is constrained to minimize postshock oscillations. In the cosmological setting, the TVD-based codes include those of Ryu et al. (1993), the moving-mesh scheme (Pen 1998), and the smooth Lagrangian method (Gnedin 1995); and the PPM-based

[1] Purple Mountain Observatory, Chinese Academy of Sciences, 2 Beijing Xi Lu, Nanjing, Jiangsu 210008, China; fengll@pmo.ac.cn.
[2] Center for Astrophysics, University of Science and Technology of China, 96 Jinzai Lu, Hefei, Anhui 230026, China.
[3] National Astronomical Observatories, Chinese Academy of Sciences, A20 Datun Road, Chao-Yang District, Beijing 100012, China.
[4] Division of Applied Mathematics, Brown University, Providence, RI 02912; shu@dam.brown.edu.
[5] Department of Mathematics, University of Science and Technology of China, Hefei, Anhui 230026, China; mpzhang@ustc.edu.cn.

codes include those of Stone & Norman (1992; Zeus), Bryan et al. (1995), Sornborger et al. (1996), and Ricker et al. (2000; COSMOS). The grid-based methods suffer from limited spatial resolution, but they work extremely well in both low- and high-density regions, as well as in shocks. To reach a large dynamical range, the Godunov methods have also been implemented with adaptive mesh refinement (RAMSES, Teyssier 2002; ENZO, Norman & Bryan 1999; O'Shea et al. 2004), which is more adequate to explore the fine structures in the hydrodynamic simulation.

We describe in this paper an alternative hydrodynamic solver that discretizes the convection terms in the Euler equations by the fifth-order finite difference weighted essentially non-oscillatory (WENO) method, first developed in Jiang & Shu (1996), with a low-storage third-order Runge-Kutta time discretization, which was proven to be nonlinearly stable in Gottlieb & Shu (1998). The WENO schemes are based on the essentially nonoscillatory (ENO) schemes first developed by Harten et al. (1987) in the form of finite volume scheme for hyperbolic conservative laws. The ENO scheme generalizes the TVD scheme of Harten (1983). The TVD schemes typically degenerate to first-order accuracy at locations with smooth extrema, while the ENO scheme maintains high-order accuracy there even in multiple dimensions. WENO schemes further improve on ENO schemes in robustness and accuracy. Both ENO and WENO schemes use the idea of adaptive stencils in the reconstruction procedure based on the local smoothness of the numerical solution to automatically achieve high-order accuracy and nonoscillatory property near discontinuities. For WENO schemes, this is achieved by using a convex combination of a few candidate stencils, each being assigned a nonlinear weight that depends on the local smoothness of the numerical solution based on that stencil. WENO schemes can simultaneously provide a high-order resolution for the smooth part of the solution and a sharp, monotone shock or contact discontinuity transition. WENO schemes are extremely robust and stable for solutions containing strong shocks and complex solution structures. Moreover, a significant advantage of WENO is its ability to have high accuracy on coarser meshes and to achieve better resolution on the largest meshes allowed by available computer memory. We describe the fifth-order WENO scheme employed in this paper briefly in § 3. For more details, we refer to Jiang & Shu (1996) and the lecture notes by Shu (1998, 1999).

WENO schemes have been widely used in applications. Some examples include dynamical response of a stellar atmosphere to pressure perturbations (Del Zanna et al. 1998), shock vortex interactions and other gasdynamic problems (Grasso & Pirozzoli 2000a, 2000b), incompressible flow problems (Yang et al. 1998), Hamilton-Jacobi equations (Jiang & Peng 2000), magnetohydrodynamics (Jiang & Wu 1999), underwater blast wave focusing (Liang & Chen 1999), composite schemes and shallow water equations (Liska & Wendroff 1998, 1999), real gas computations (Montarnal & Shu 1999), and wave propagation using Fey's method of transport (Noelle 2000).

In the context of cosmological applications, we have developed a hybrid N-body/hydrodynamical code that incorporates a Lagrangian particle-mesh algorithm to evolve the collisionless matter with the fifth-order WENO scheme to solve the equations of gasdynamics. The purpose of this paper is to detail this code and assess its accuracy using some numerical tests. We proceed as follows. In § 2 we present the basic cosmological hydrodynamic equation for the baryon-CDM coupling system. In § 3 we give a brief discussion of the numerical scheme for solving the hydrodynamic equations, especially concerning the implementation of the finite difference fifth-order WENO scheme and the TVD time discretization. In § 4 we validate the code using a few challenging numerical tests. Concluding remarks are made in § 5.

2. THE BASIC EQUATIONS

The hydrodynamic equations for baryons in the expanding universe, without any viscous and thermal conductivity terms, can be written in the compact form

$$U_t + f(U)_X + g(U)_Y + h(U)_Z = F(t, U), \qquad (1)$$

where U and the fluxes $f(U)$, $g(U)$, and $h(U)$ are five-component column vectors,

$$\begin{pmatrix} \rho \\ \rho u \\ \rho v \\ \rho w \\ E \end{pmatrix}, \quad \begin{pmatrix} \rho u \\ \rho u^2 + P \\ \rho uv \\ \rho uw \\ u(E+P) \end{pmatrix}, \quad \begin{pmatrix} \rho v \\ \rho uv \\ \rho v^2 + P \\ \rho vw \\ v(E+P) \end{pmatrix}, \quad \begin{pmatrix} \rho w \\ \rho uw \\ \rho vw \\ \rho w^2 + P \\ w(E+P) \end{pmatrix}.$$
$$(2)$$

Here t is the cosmic time and $\boldsymbol{R} = (X, Y, Z)$ are the proper coordinates, which are related to comoving coordinates $\boldsymbol{r} = (x, y, z)$ via $\boldsymbol{R} = a(t)\boldsymbol{r}$. The subscripts (X, Y, Z) in equation (1) denote spatial derivatives, e.g., $(\cdot)_X = \partial(\cdot)/\partial X$; $a(t)$ is the expansion scale factor, ρ is the comoving density, $\boldsymbol{V} = (u, v, w)$ is the proper peculiar velocity, E is the total energy including both kinetic and internal energies, and P is comoving pressure, which is related to the total energy E by

$$E = \frac{P}{\gamma - 1} + \frac{1}{2}\rho(u^2 + v^2 + w^2), \qquad (3)$$

where we assume an ideal gas equation of state, $P = (\gamma - 1)e$, where e is the total internal energy and γ is the ratio of the specific heats of the baryon; for a monatomic gas, $\gamma = 5/3$. The left-hand side of equation (1) is written in the conservative form for mass, momentum, and energy, and the "force" source term on the right-hand side includes the contributions from the expansion of the universe and the gravitation:

$$\begin{pmatrix} 0 \\ -\dfrac{\dot{a}}{a}\rho\boldsymbol{V} + \rho\boldsymbol{G} \\ -2\dfrac{\dot{a}}{a}E + \rho\boldsymbol{V}\cdot\boldsymbol{G} - \Lambda_{\mathrm{net}} \end{pmatrix}, \qquad (4)$$

where Λ_{net} represents the net energy loss due to the radiative heating-cooling of the baryonic gas and $\boldsymbol{G} = -\nabla_R\Phi$ is the peculiar acceleration in the gravitational field produced by both the dark matter and the baryonic matter.

The motions of the collisionless dark matter in comoving coordinates are governed by a set of Newtonian equations,

$$\frac{d\boldsymbol{r}_{\mathrm{DM}}}{dt} = \frac{1}{a}\boldsymbol{v}_{\mathrm{DM}},$$
$$\frac{d\boldsymbol{v}_{\mathrm{DM}}}{dt} = -\frac{\dot{a}}{a}\boldsymbol{v}_{\mathrm{DM}} + \boldsymbol{G}, \qquad (5)$$

where $\boldsymbol{r}_{\mathrm{DM}}$ and $\boldsymbol{v}_{\mathrm{DM}}$ are the comoving coordinates and the proper peculiar velocity, respectively, and the subscript DM refers to the dark matter. The peculiar gravitational potential obeys the Poisson equation,

$$\nabla^2 \Phi(\boldsymbol{x},\ t) = 4\pi G[\rho_{\mathrm{tot}}(\boldsymbol{x},\ t) - \rho_0(t)]/a, \qquad (6)$$

in which G is the gravitational constant, $\rho_{\mathrm{tot}} = \rho_b + \rho_{\mathrm{DM}}$ is a sum of the comoving baryon and dark matter density, and $\rho_0(t)$ is the uniform background density at time t.

3. NUMERICAL TECHNIQUES

3.1. Hydrodynamic Solver: Finite Difference WENO Schemes

3.1.1. Approximating the Derivatives

The fifth-order WENO finite difference spatial discretization to a conservation law such as

$$u_t + f(u)_x + g(u)_y + h(u)_z = 0 \qquad (7)$$

approximates the derivatives, for example, $f(u)_x$, by a conservative difference

$$f(u)_x|_{x=x_j} \approx \frac{1}{\Delta x} \left(\hat{f}_{j+1/2} - \hat{f}_{j-1/2} \right)$$

along the x line, with y and z fixed, where $\hat{f}_{j+1/2}$ is the numerical flux; $g(u)_y$ and $h(u)_z$ are approximated in the same way. Hence, finite difference methods have the same format for one and several space dimensions, which is a major advantage. For the simplest case of a scalar equation (7) and if $f'(u) \geq 0$, the fifth-order finite difference WENO scheme has the flux given by

$$\hat{f}_{j+1/2} = w_1\, \hat{f}^{(1)}_{j+1/2} + w_2\, \hat{f}^{(2)}_{j+1/2} + w_3\, \hat{f}^{(3)}_{j+1/2},$$

where $\hat{f}^{(i)}_{j+1/2}$ are three third-order accurate fluxes on three different stencils given by

$$\hat{f}^{(1)}_{j+1/2} = \frac{1}{3}f(u_{j-2}) - \frac{7}{6}f(u_{j-1}) + \frac{11}{6}f(u_j),$$
$$\hat{f}^{(2)}_{j+1/2} = -\frac{1}{6}f(u_{j-1}) + \frac{5}{6}f(u_j) + \frac{1}{3}f(u_{j+1}),$$
$$\hat{f}^{(3)}_{j+1/2} = \frac{1}{3}f(u_j) + \frac{5}{6}f(u_{j+1}) - \frac{1}{6}f(u_{j+2}).$$

Note that the combined stencil for the flux $\hat{f}_{j+1/2}$ is biased to the left, which is upwinding for the positive wind direction as a result of the assumption $f'(u) \geq 0$. The key ingredient for the success of the WENO scheme relies on the design of the nonlinear weights w_i, which are given by

$$w_i = \frac{\tilde{w}_i}{\sum_{k=1}^{3} \tilde{w}_k}, \quad \tilde{w}_k = \frac{\gamma_k}{(\varepsilon + \beta_k)^2},$$

where the linear weights γ_k are chosen to yield fifth-order accuracy when combining three third-order accurate fluxes and are given by

$$\gamma_1 = \frac{1}{10}, \quad \gamma_2 = \frac{3}{5}, \quad \gamma_3 = \frac{3}{10}.$$

The smoothness indicators β_k are given by

$$\beta_1 = \frac{13}{12}\left[f(u_{j-2}) - 2f(u_{j-1}) + f(u_j)\right]^2$$
$$+ \frac{1}{4}\left[f(u_{j-2}) - 4f(u_{j-1}) + 3f(u_j)\right]^2,$$
$$\beta_2 = \frac{13}{12}\left[f(u_{j-1}) - 2f(u_j) + f(u_{j+1})\right]^2$$
$$+ \frac{1}{4}\left[f(u_{j-1}) - f(u_{j+1})\right]^2,$$
$$\beta_3 = \frac{13}{12}\left[f(u_j) - 2f(u_{j+1}) + f(u_{j+2})\right]^2$$
$$+ \frac{1}{4}\left[3f(u_j) - 4f(u_{j+1}) + f(u_{j+2})\right]^2,$$

and they measure how smooth the approximation based on a specific stencil is in the target cell. Finally, ε is a parameter to keep the denominator from becoming 0 and is usually taken as $\varepsilon = 10^{-6}$ in the computation. The choice of ε does not affect accuracy; the errors can go down to machine zero with mesh refinement while $\varepsilon = 10^{-6}$ is kept fixed.

This finishes the description of the fifth-order finite difference WENO scheme in Jiang & Shu (1996) in the simplest case. As we can see, the algorithm is actually quite simple and the user does not need to tune any parameters in the scheme.

3.1.2. Properties of the WENO Scheme

We briefly summarize the properties of this WENO finite difference scheme (for details of proofs and numerical verifications see Jiang & Shu 1996 and the lecture notes of Shu 1998, 1999):

1. The scheme is proven to be uniformly fifth-order accurate including at smooth extrema, and this is verified numerically.

2. Near discontinuities the scheme produces a sharp and nonoscillatory discontinuity transition.

3. The approximation is self-similar. That is, when fully discretized with the Runge-Kutta methods in the next section, the scheme is invariant when the spatial and time variables are scaled by the same factor. This is a major advantage for approximating conservation laws that are invariant under such scaling.

3.1.3. Generalization to More Complex Situations

We then indicate how the scheme is generalized in a more complex situation, eventually to three-dimensional systems such as the Euler equations:

1. For scalar equations without the property $f'(u) \geq 0$, one uses a flux splitting

$$f(u) = f^+(u) + f^-(u), \quad \frac{df^+(u)}{du} \geq 0, \quad \frac{df^-(u)}{du} \leq 0$$

and applies the above procedure to $f^+(u)$ and a mirror image (with respect to $j + \frac{1}{2}$) procedure to $f^-(u)$. The only requirement for the splitting is that $f^\pm(u)$ should be smooth functions of u. In this paper we use the simple Lax-Friedrichs flux splitting,

$$f^\pm(u) = \tfrac{1}{2}\left[f(u) \pm \alpha u\right], \qquad \alpha = \max_u |f'(u)|,$$

where the maximum is taken over the relevant range of u. This simple Lax-Friedrichs flux splitting is quite diffusive when applied to first- and second-order discretizations, but for the fifth-order WENO discretization we adopt, it has very small numerical viscosity.

2. For systems of hyperbolic conservation laws, the nonlinear part of the WENO procedure (i.e., the determination of the smoothness indicators β_k and hence the nonlinear weights w_i) is carried out in local characteristic fields. Thus, one would first find an average $u_{j+1/2}$ of u_j and u_{j+1} (we use the Roe average [Roe 1978], which exists for many physical systems including the Euler equations), compute the left and right eigenvectors of the Jacobian $f'(u_{j+1/2})$, and put them into the rows of a matrix $R_{j+1/2}^{-1}$ and the columns of another matrix $R_{j+1/2}$, respectively, such that $R_{j+1/2}^{-1} f'(u_{j+1/2}) R_{j+1/2} = \Lambda_{j+1/2}$, where $\Lambda_{j+1/2}$ is a diagonal matrix containing the real eigenvalues of $f'(u_{j+1/2})$. One then transforms all the quantities needed for evaluating the numerical flux $\hat{f}_{j+1/2}$ to the local characteristic fields by left multiplying them with $R_{j+1/2}^{-1}$ and then computes the numerical fluxes by the scalar procedure in each characteristic field. Finally, the flux in the original physical space is obtained by left multiplying the numerical flux obtained in the local characteristic fields with $R_{j+1/2}$.

3. If one has a nonuniform but smooth mesh, for example, $x = x(\xi)$, where ξ_j is uniform and $x(\xi)$ is a smooth function of ξ, then one could use the chain rule $f(u)_x = f(u)_\xi / x'(\xi)$ and simply use the procedure above for uniform meshes to approximate $f(u)_\xi$. Using this, one could use finite difference WENO schemes on smooth curvilinear coordinates in any space dimension.

4. WENO finite difference schemes are available for all odd orders; see Liu et al. (1994) and Balsara & Shu (2000) for the formulae of the third-order and seventh- through eleventh-order WENO schemes.

3.2. *Time Discretizations*

The finite-difference WENO scheme we use in this paper is formulated first as a method of lines, namely, discretized in the spatial variables only. It is still necessary for us to discretize the time variable. Often it is easier to prove stability (e.g., for TVD schemes) when the time variable is discretized by the first-order accurate forward Euler; however, time accuracy is as important as spatial accuracy; hence, we would like to have higher order accuracy in time while maintaining the stability properties of the forward Euler time stepping. We use a class of high-order nonlinearly stable Runge-Kutta time discretizations. A distinctive feature of this class of time discretizations is that they are convex combinations of first-order forward Euler steps; hence, they maintain strong stability properties in any seminorm (total variation norm, maximum norm, entropy condition, etc.) of the forward Euler step, with a time step restriction proportional to that for the forward Euler step to be stable, this proportion coefficient being termed the CFL (Courant-Friedrichs-Levy, referring to stability restrictions on the time step) coefficient of the high-order Runge-Kutta method. Thus, one only needs to prove nonlinear stability for the first-order forward Euler step, which is relatively easy in many situations (e.g., TVD schemes), and one automatically obtains the same strong stability property for the higher order time discretizations in this class. These methods were first developed in Shu & Osher (1988) and Shu (1988) and later generalized in Gottlieb & Shu (1998) and Gottlieb et al. (2001).

The most popular scheme in this class is the following third-order Runge-Kutta method for solving

$$u_t = L(u, \, t),$$

where $L(u, \, t)$ is a spatial discretization operator (it does not need to be, and often is not, linear):

$$
\begin{aligned}
u^{(1)} &= u^n + \Delta t L(u^n, \, t^n), \\
u^{(2)} &= \tfrac{3}{4} u^n + \tfrac{1}{4} u^{(1)} + \tfrac{1}{4} \Delta t L\left(u^{(1)}, \, t^n + \Delta t\right), \\
u^{n+1} &= \tfrac{1}{3} u^n + \tfrac{2}{3} u^{(2)} + \tfrac{2}{3} \Delta t L\left(u^{(2)}, \, t^n + \tfrac{1}{2} \Delta t\right),
\end{aligned}
\tag{8}
$$

which is nonlinearly stable with a CFL coefficient 1. However, for our purpose of three-dimensional calculations, storage is a paramount consideration. We thus use a third-order low-storage nonlinearly stable Runge-Kutta method, which was proven to be nonlinearly stable with a CFL coefficient 0.32 (Gottlieb & Shu 1998). Although the time step of this low-storage method must be smaller for stability analysis, in practice the time step can be larger (for example, with a CFL coefficient 0.6 used in this paper) without observing any instability. In the Appendix, the algorithm of the third-order low-storage Runge-Kutta method is given. This method is to be applied to the numerical tests presented in § 4.

3.3. *Resolving the High Mach Number Problem*

In cosmological hydrodynamic simulations, one main challenge is to track precisely the thermodynamic evolution in supersonic flows around the density peaks due to gravitational collapse. The supersonic flow could have a high Mach number, as large as $M \sim 100$, at which the ratio of the internal thermal energy $E_{\rm th}$ to the kinetic energy E_k is as small as $M^{-2} \sim 10^{-4}$. In an Eulerian numerical scheme for hydrodynamics, the thermal energy is obtained by subtracting the kinetic energy from the total energy $E_{\rm th} = E - E_k$. This calculation leads to a significant error if the thermal energy is negligibly small compared to the kinetic energy. Even though there is an improvement of the quality when the WENO scheme is used, due to its high-order accuracy near shock fronts, the problem still remains. This is what is referred to in the literature as the high Mach number problem.

To tackle the high Mach number flow that frequently appears in cosmological hydrodynamic simulations, the current common practice is to solve the thermal energy accurately using a complementary equation in the unshocked region, either a modified entropy equation (Ryu et al. 1993) or the internal energy equation (Bryan et al. 1995). In this paper we combine these two approaches. That is, we take the dual-energy approach of Bryan et al. (1995), but instead of solving the internal energy equation, we follow Ryu et al. (1993) to solve the modified entropy equation. Without taking into account the energy loss across shocks, the conservative form of the modified entropy is

$$\frac{\partial S}{\partial t} + \frac{1}{a} \nabla \cdot (S \boldsymbol{V}) = -2 \frac{\dot{a}}{a} S, \tag{9}$$

where S is the modified entropy defined by $S \equiv p / \rho^{\gamma-1}$. We note that the entropy equation is only valid in unshocked regions and can be solved numerically by the standard WENO
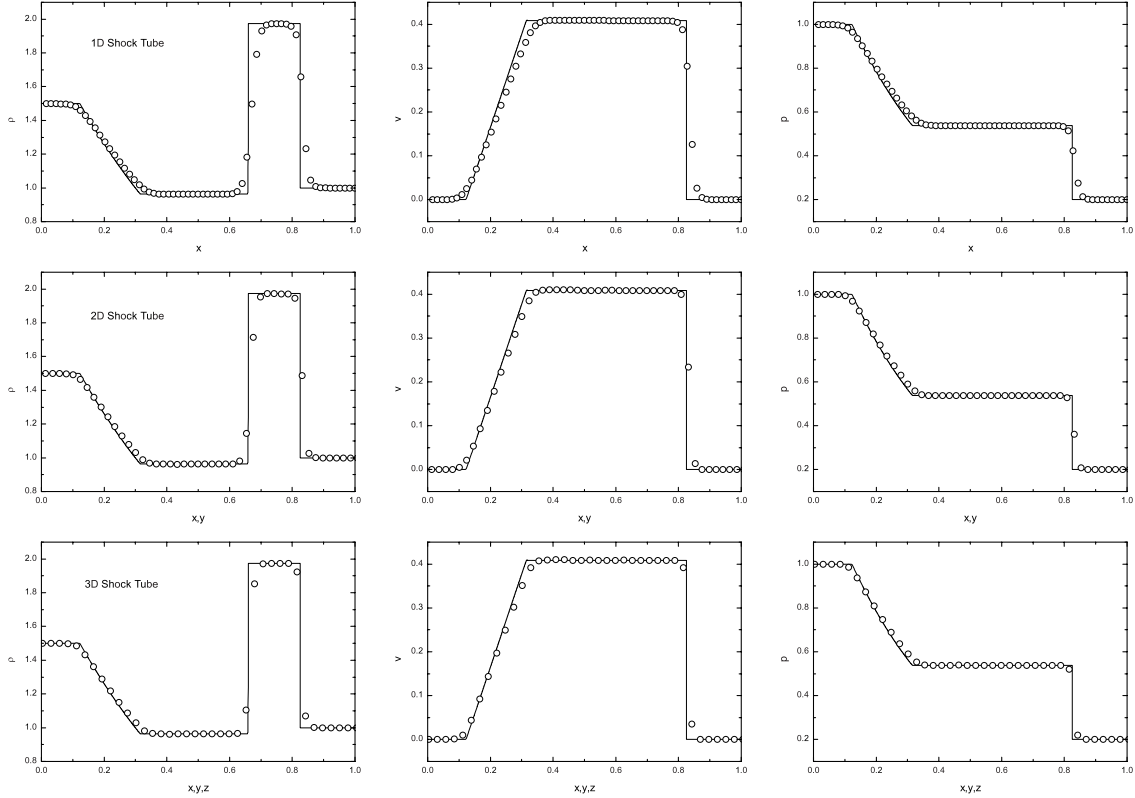
Fig. 1.—Density (*left*), velocity (*middle*), and pressure (*right*) for the Sod shock tube tests in one, two, and three dimensions. Open circles are given by the numerical solution output at $t = 0.195$ using the fifth-order WENO scheme; solid lines represent the analytical solutions.

finite difference scheme. With the entropy equation (9), the thermal energy is updated from the results of either total energy inside shocks or modified entropy outside shocks according to an ad hoc criterion, which operates on each cell using

$$
p = \begin{cases} (\gamma - 1)\left(E - \dfrac{1}{2}\rho v^2\right), & \dfrac{E - (1/2)\rho v^2}{E} \geq \eta, \\[2ex] S\rho^{\gamma-1}, & \dfrac{E - (1/2)\rho v^2}{E} < \eta, \end{cases} \quad (10)
$$

where η is a free parameter. We take $\eta = 10^{-3}$ in our calculations in order to have no noticeable dynamical effect on the system. To incorporate the pressure obtained from the modified entropy equation into the total energy equation, we reset the total energy E or the entropy S at each time loop. Namely, according to the criterion equation (10), if the pressure is determined by the total energy equation, we update the entropy by $S = p/\rho^{\gamma-1}$, and if the pressure is given by the entropy equation, we reset the total energy by $E = p/(\gamma - 1) + \rho v^2/2$. These procedures enable us to track both the thermal energy and total energy correctly in the shocked and unshocked regions.

3.4. *Implementation*

In practical cosmological simulations, the code proceeds according to the following stages:

1. Under the Gaussian assumption of the primordial density fluctuations, we initialize a simulation using the Zel'dovich approximation to set up a distribution of CDM particles. The baryonic density and velocity fields are then given as in Cen (1992).

2. The WENO scheme is applied to compute the advection fluxes for the hydrodynamic variables as described in § 3.1.

3. The gravitational field is solved by the standard particle-mesh N-body technique (see Hockney & Eastwood 1988; Efstathiou et al. 1985). Namely, for the dark matter particles, the density is assigned to the grid with a cloud-in-cell (CIC) method and then subjected to a fast Fourier transform (FFT) to generate the discretized density field; the gravitational potential to the Poisson equation is then obtained by a convolution technique, in which we make use of the optimized Green's function appropriate to the seven-point finite difference approximation to the Laplacian.

4. The positions and velocities of CDM particles, as well as the hydrodynamic variables, are updated with the third-order low-storage Runge-Kutta method, which ensures third-order accuracy in the time integration of the system.

The time step is chosen by the minimum value among three timescales. The first is from the Courant condition given by

$$
\Delta t \leq \frac{\text{CFL}[a(t)\Delta x]}{\max\left(|u_x| + c_s, \ |u_y| + c_s, \ |u_z| + c_s\right)}, \quad (11)
$$

where Δx is the cell size, c_s is the local sound speed, u_x, u_y, and u_z are the local fluid velocities, and CFL is the Courant number for the stability of time discretization. The analysis for nonlinear stability allows the Courant number to be up to 1 for the regular third-order nonlinearly stable Runge-Kutta time discretization given by equation (8) and up to 0.32 for the
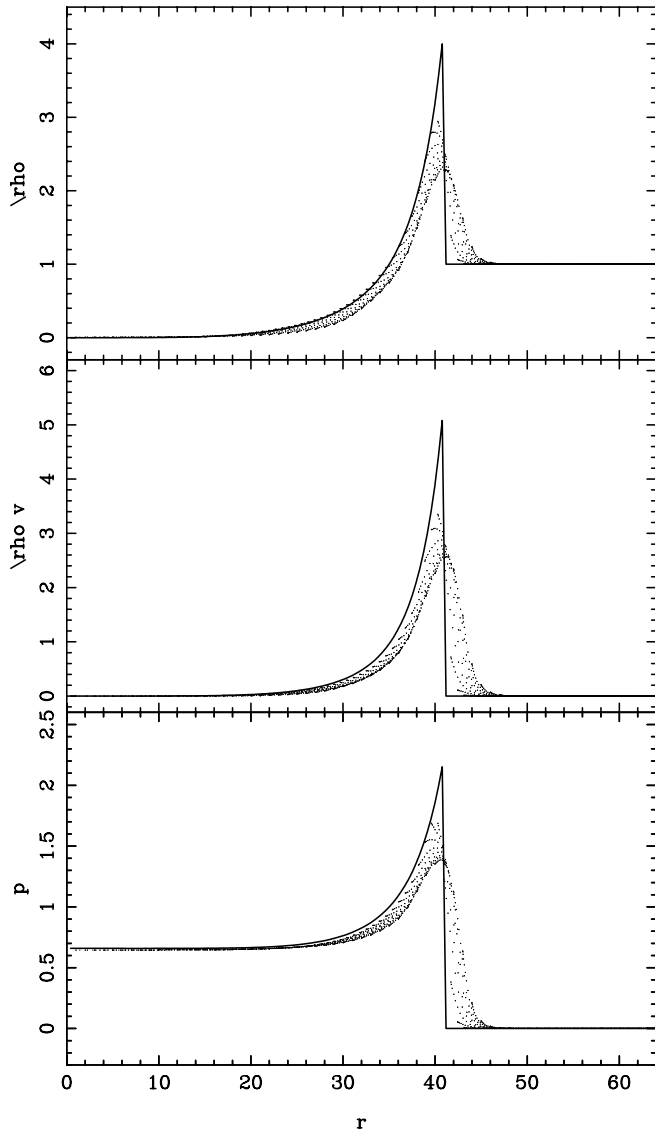
FIG. 2.—Density (*top*), momentum density (*middle*), and pressure (*bottom*) in the three-dimensional spherical Sedov blast wave test at $t = 9.22$. The computation is performed on a 256^3 grid, and the scattered points are plotted by the projection of the results on the Cartesian grids onto the spherical radial coordinates. The solid lines represent the analytical solutions.

FIG. 3.—Gray image of density distribution in a slice across the explosion point in the three-dimensional spherical Sedov blast wave at $t = 9.22$.

low-storage third-order nonlinearly stable Runge-Kutta time discretization given by equations (A1) and (A2), which we use in this paper. Typically, we take CFL = 0.6 in our computation and observe stable results. The second constraint is imposed by cosmic expansion, which requires that $\Delta a/a < 0.02$ within a single time step. This constraint comes from the requirement that a particle moves no more than a fixed fraction of the cell size in one time step. In cosmological simulations, the time step is always controlled by the cosmological expansion at the early stage of evolution, but most of the CPU time is spent in Courant time steps at the later nonlinear clustering regimes.

Our hybrid cosmological hydrodynamic/N-body code has been written in FORTRAN 90. Compiling on a Dell precision 530 workstation with one Intel(R) Xeon(TM) Processor 2.8 GHz/533 MHz, it runs at the speed of $\sim 1.9 \times 10^4$ zones s^{-1} without the N-body/gravity solver and $\sim 1.6 \times 10^4$ zones s^{-1} with the N-body/gravity solver. For the benchmark of the WENO code with the same implementation as ours but without gravity, performed on an IBM SP parallel computer,
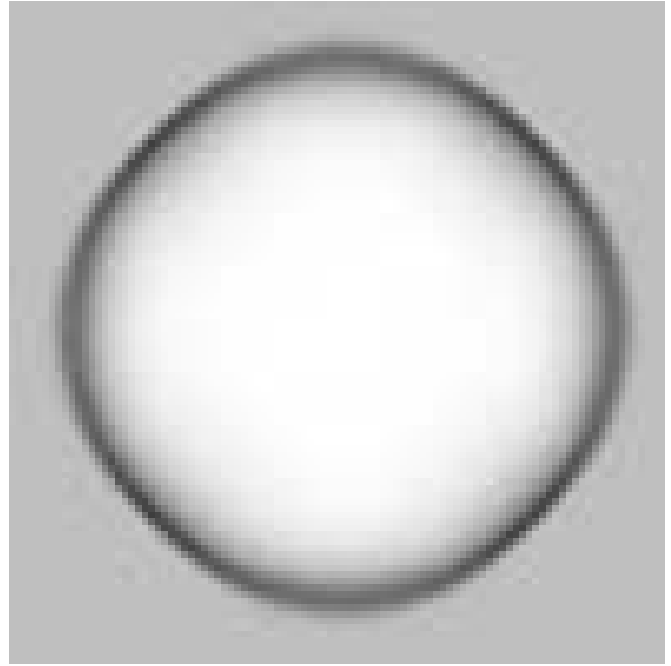
we refer the reader to Tables 1 and 2 of Shi et al. (2003) for details.

4. NUMERICAL TESTS

The WENO scheme in application to both compressible and incompressible gas hydrodynamics has been subjected to a variety of numerical tests, such as the shock tube problem, double Mach reflection, two-dimensional shock vortex inter-actions, etc. All of these tests work very well, especially for the situation in which both shocks and complicated smooth flow features coexist, demonstrating the advantages of high-order schemes. For these test results of WENO schemes, see, e.g., Shu (2003) and references therein. In this section we are going to run the following tests: (1) the Sod shock tube tests in one, two, and three dimensions; (2) the Sedov spherical blast wave in three dimensions; (3) the Zel'dovich pancake, which characterizes the structure formation in the universe by the single-mode analysis; and (4) finally, we demonstrate the code by simulating the adiabatic evolution of the universe in a ΛCDM model.

4.1. *Shock Tube Test*

The Sod shock tube problem (Sod 1978) has been widely used to test the ability of hydrodynamic codes for shock capturing. Under a specifically chosen initial condition, it could produce all of three types of fluid discontinuity: shock, contact, and rarefaction. The Sod problem is set as a straight tube of gas divided by a membrane into two chambers. The initial state of the gas is specified by uniform density and pressure on both chambers, respectively. On the left chamber, we set $\rho_L = 1.5$, $p_L = 1.0$, and on the right, $\rho_R = 1.0$, $p_R = 0.2$. The gas is assumed to be at rest everywhere initially. The polytropic index is $\gamma = 1.4$.

The Sod shock tube is actually a one-dimensional problem. To find how well the shock structure is resolved in high dimensions, we perform the test in one-, two-, and three-dimensional cases. In one dimension, the shock propagates along the line of the x-axis. For two- and three-dimensional cases, the shock propagates along the main diagonal of the
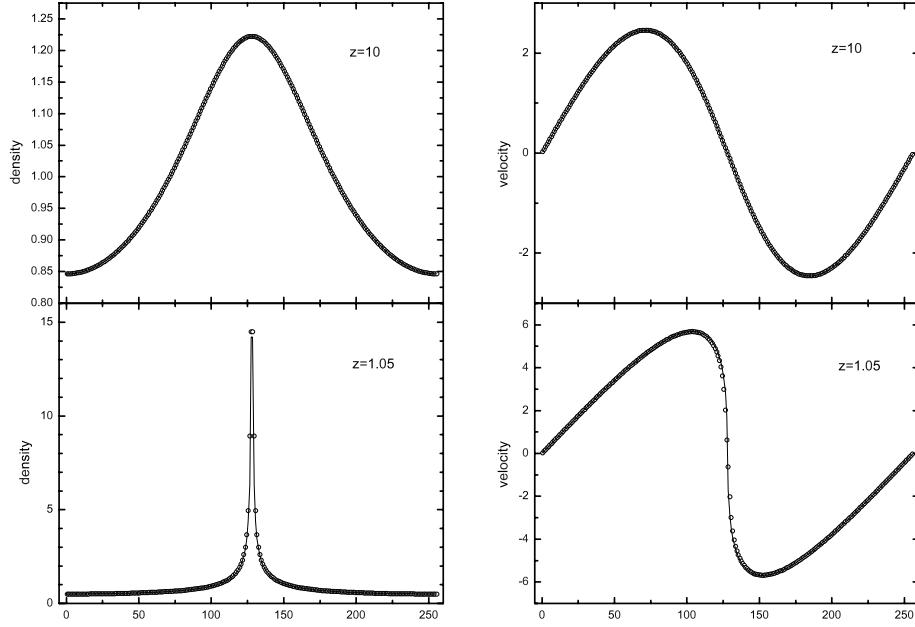
Fig. 4.—One-dimensional Zel'dovich pancake test at redshifts $z = 10$ and 1.05 prior to the caustics formation. The results from a 256 grid run (*open circles*) are plotted against the exact solutions (*solid line*).

calculation region, i.e., along the line $(0, 0)$ to $(1, 1)$ in the square and along the line $(0, 0, 0)$ to $(1, 1, 1)$ in the cube. Figure 1 compares the numerical results at $t = 0.195$ with the analytical solution in one, two, and three dimensions, respectively, in which 64 cells in each direction have been used. Comparable to the calculations made with PPM or TVD schemes (e.g., Ryu et al. 1993; Pen 1998; Ricker et al. 2000), the shock and contact discontinuity can be resolved within two to three cells in the multidimensional calculations, and moreover, each quantity gets some improvements with the increase of spatial dimensions.

4.2. *Spherical Sedov-Taylor Blast Wave*

Another challenging test for the three-dimensional hydrodynamic code is the Sedov blast wave (Sedov 1993). We initialize the simulation by setting up a pointlike energy release in a homogeneous medium of density and negligible pressure. This explosion will develop a spherical blast wave that sweeps material around as it propagates outward along the radial direction. The derivation of the full analytical solutions can be found in Landau & Lifshitz (1987). It has been currently used for modeling the supernova explosion.

The shock front propagates according to

$$r_s(t) = \xi_0 \left(\frac{E_0 t^2}{\rho_1} \right)^{1/5}, \qquad (12)$$

where $\xi_0 = 1.15$ for an ideal gas with a polytropic index $\gamma = 5/3$. The velocity of the shock is given by $v_s = \partial r_s(t)/\partial t$. Behind the shock, the density, momentum, and pressure are given by

$$\rho_2 = \frac{\gamma + 1}{\gamma - 1} \rho_1, \qquad (13)$$

$$(\rho v)_2 = \frac{2}{\gamma - 1} \rho_1 v_s, \qquad (14)$$

$$P_2 = \frac{2}{\gamma + 1} \rho_1 v_s^2. \qquad (15)$$

We apply the three-dimensional WENO scheme to run the Sedov-Taylor blast test. The simulation is performed in a cubic box with a 256^3 grid and initialized by setting up a uniform density $\rho_1 = 1$ and negligible pressure with a very small value $p_0 = 10^{-5}$ to match a numerical approximation to zero. A pointlike energy $E_0 = 10^5$ is injected at the center of the box, and the medium is at rest initially. The challenging nature of the spherical Sedov-Taylor blast wave stems from the fact that a Cartesian grid is used. To minimize the anisotropic effects due to the Cartesian coordinates, we convolve the initial condition with a spherical Gaussian filter with a window radius of 1.5 grids.

The full three-dimensional numerical solutions for density, momentum, and pressure are displayed in Figure 2 by projecting onto the radial coordinate. As can be seen in Figure 2, the numerical solution captures the spatial profile of the shock well, although there is still some scattering around the analytical solution. Obviously, the scattering originates from the geometric effect of the projection from the Cartesian grid onto the spherical coordinate. Such geometric anisotropy also leads to the shock front being not fully resolved within one cell as described by the analytical solution. Accordingly, in the widened shock front of the numerical solution, both density and pressure have been underestimated in comparison with their predicted maximum values. Figure 3 presents the density distributions in a slice across the explosion point. The anisotropy could be clearly seen in this figure.

4.3. *Zel'dovich Pancake*

The Zel'dovich pancake problem (Zel'dovich 1970) provides a stringent numerical test for cosmological hydrodynamic codes. It involves the basic physics underlying cosmological simulation, namely, hydrodynamics, self-gravity, cosmic expansion, and strong shock formed in smooth structure with high Mach numbers. In the one-dimensional case, the problem can be formulated by placing a sinusoidal perturbation along the axis and tracking its evolution. In the linear or quasi-linear regime, there exists an exact solution in the Lagrangian
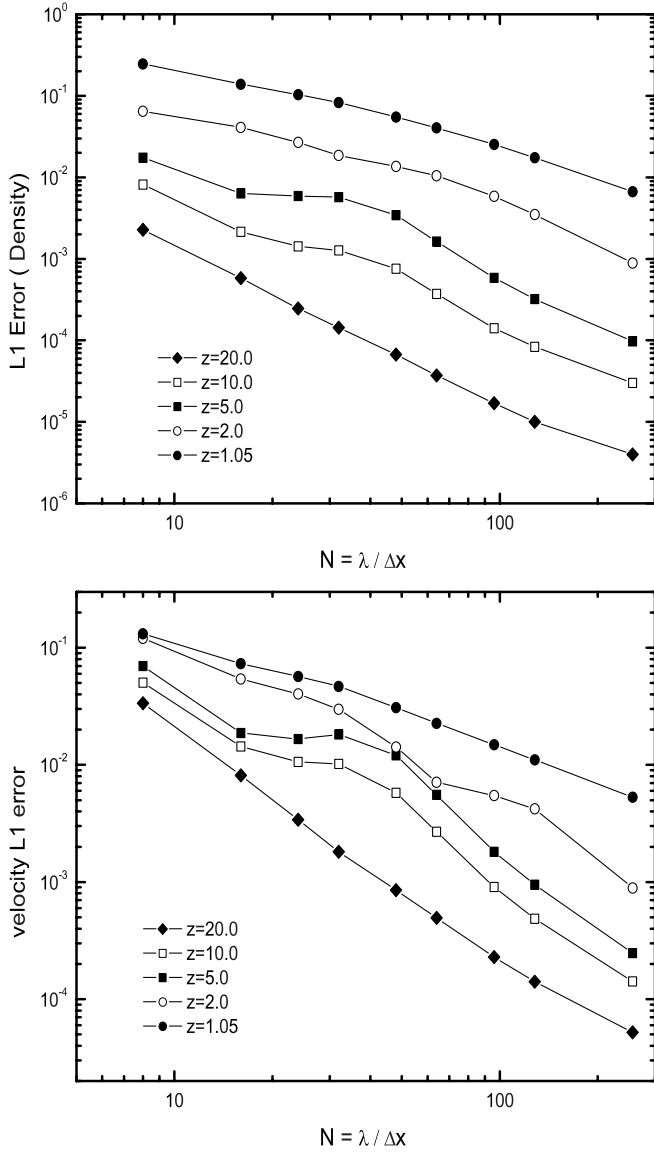
Fig. 6.—Density (*top*), velocity (*middle*), and temperature (*bottom*) for a one-dimensional Zel'dovich pancake at redshift $z = 0$. The results are drawn from a 256 grid run.

Fig. 5.—L^1 error norm of one-dimensional Zel'dovich pancake tests varying with the number of zones N for a fixed perturbation wavelength. The results for density (*top*) and velocity (*bottom*) are plotted at different redshifts.

coordinate if the pressure is neglected. For a flat cosmology, the solution can be written in the following forms:

$$\rho(x_l) = \rho_0 \left[1 - \frac{1+z_c}{1+z} \cos(kx_l) \right]^{-1}, \qquad (16)$$

$$v(x_l) = -H_0 \frac{1+z_c}{(1+z)^{1/2}} \frac{\sin(kx_l)}{k}, \qquad (17)$$

where z_c is a redshift at which the gravitational collapse results in the formation of caustics, i.e., Zel'dovich pancake. H_0 is the Hubble constant, $H_0 = 100 \, h$ km s^{-1} Mpc^{-1}, and $k = 2\pi/\lambda$ specifies the comoving perturbation wavelength. Furthermore, x_l is the Lagrangian coordinate, which is related to the Eulerian position x_e by

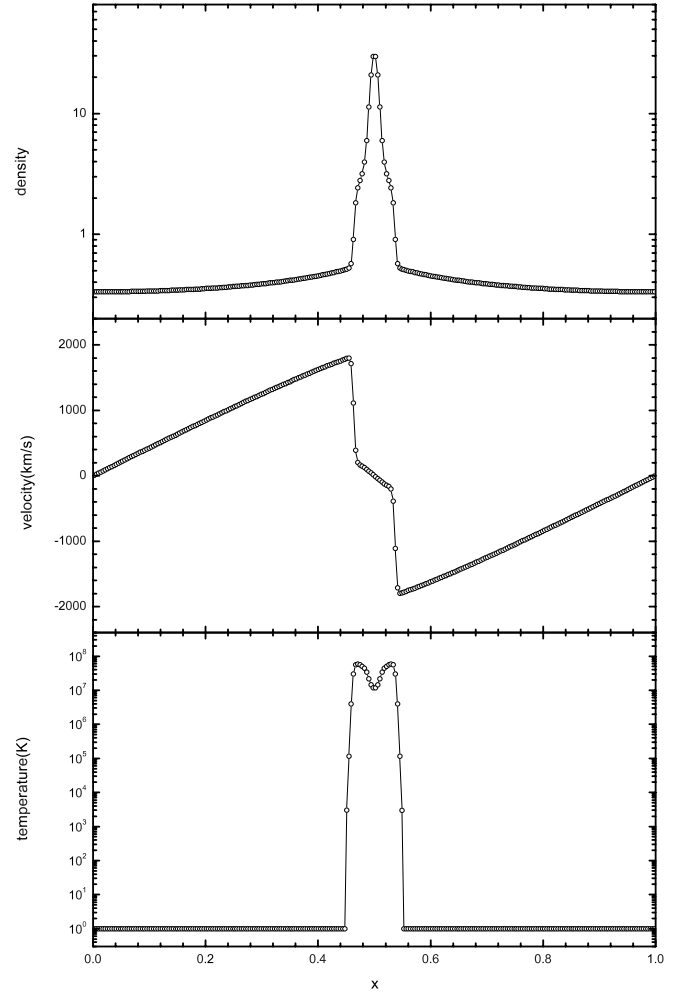$$x_l - \frac{1+z_c}{1+z} \frac{\sin(kx_l)}{k} = x_e. \qquad (18)$$

For the numerical model, we adopt the same parameters as those used in Bryan et al. (1995), which are given by $z_c = 1$, $\Omega = 1$, $h = 0.5$, and $\lambda = 64 \, h^{-1}$ Mpc. The simulation is performed from the initial redshift $z_i = 100$ for the purely baryonic gas with a uniform temperature distribution $T_i = 100$ K.

We note that the analytical solution given by equation (16) holds until the redshift $z = z_c$ of caustic formation. In Figure 4 we compare the numerical solution using a 256 grid to the Zel'dovich pancake with the analytical solution at $z = 10$ and 1.05. We can clearly see an excellent agreement between the numerical and analytical solutions. To access the accuracy to which our WENO/PM code is able to reach, we run the code with a fixed perturbation wavelength but a varying number of zones N. Using the exact solution given by equations (16)–(18), we define the L^1 error norms for the density as

$$\Delta\rho = \frac{1}{N} \sum_{i=1}^{N} \left| \frac{\rho_i - \rho_{\text{Zel},i}}{\rho_{\text{Zel},i}} \right|, \qquad (19)$$

where ρ_i is the numerical solution on the grid and $\rho_{\text{Zel},i}$ is the Zel'dovich solution given by equation (16). The L^1 error norm for the velocity fields is defined similarly. The results at different redshifts ranging from the linear regime $z = 20$ to the highly nonlinear collapsing phase $z = 1.05$ are displayed
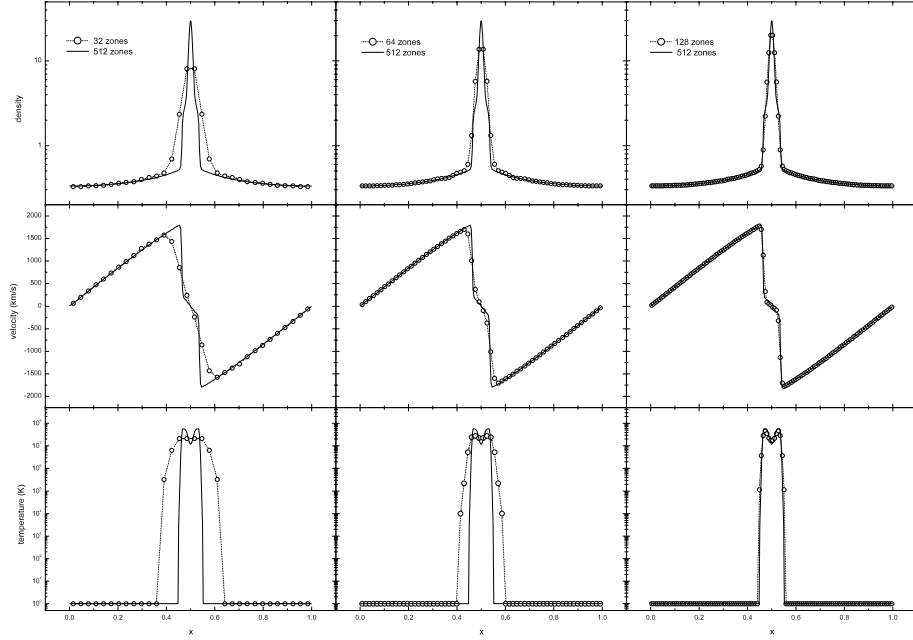
FIG. 7.—Density (*top*), velocity (*middle*), and temperature (*bottom*) for a one-dimensional Zel'dovich pancake at redshift $z = 0$. Open circles with dotted lines are obtained from the runs with 32, 64, and 128 grids. The solid lines are for the solution computed with a 512 grid run.

in Figure 5. Usually, the L^1 error should be scaled with N according to a power law $\sim N^{-r}$ or with spatial resolutions as Δx^r, where r is defined as the convergence rate. For the density field, the L^1 error declines rapidly with $r \simeq 1.8$ at $z = 20$. With decreasing redshifts, the convergence rate slows down, e.g., the error varies approximately as N^{-1} at $z = 1.05$, namely, roughly a linear convergence law with the spatial resolution. The velocity at $z = 20$ converges somewhat faster than the density with convergence rate $r \simeq 1.9$, but somewhat slower at $z = 1.05$ with $r \simeq 0.9$.

The nonlinear evolution subsequent to the caustics formation is more difficult to track numerically than that in the linear phase. The formation of the caustics is due to the head-on collision of two cold bulk flows and gravitational collapsing, which result in a strong shock and large gradients in the involved physical fields. Moreover, a large range of variation in the temperature distribution is also difficult to capture numerically. In Figure 6 we plot the solution for the density, velocity, and temperature distribution at $z = 0$ obtained from a 256 zone run. It should be noted that, in the unshocked region, the temperature is solved from the entropy equation and remains with a uniform temperature 1 K, which is the artificial minimum temperature.

To determine how well the shock is resolved by the WENO scheme at different resolutions, we also make runs with 32, 64, and 128 zones and compare with a high-resolution run with 512 zones. Unlike the similar comparison done by Bryan using the PPM scheme, we have not degraded the solution at the high resolution to appropriate scales. The results are shown in Figure 7. Clearly, the shock structure is well resolved by an approximately equal number of zones for the three low-resolution solutions, although the width of the shock is widened with reduced resolution correspondingly. Moreover, we see that the solution with 128 zones has already converged to that with 512 zones, which is likely to be the real physical solution to the problem. This demonstrates the rapid convergence rate of the high-order WENO scheme even in the highly nonlinear phase of the caustics.

4.4. *A Cosmological Application: The* ΛCDM *Model*

We run the hybrid hydrodynamic/*N*-body WENO/PM code to track the cosmic evolution of the coupled system of both dark matter and baryonic matter in a flat low-density CDM model (ΛCDM), which is specified by the density parameter $\Omega_m = 0.3$, cosmological constant $\Omega_\Lambda = 0.7$, Hubble constant $h = 0.7$, and the mass fluctuation within a sphere of radius $8\ h^{-1}$ Mpc, $\sigma_8 = 0.9$. The baryon fraction is fixed using the constraint from primordial nucleosynthesis as $\Omega_b = 0.0125\ h^{-2}$ (Walker et al. 1991). The initial condition has been generated by the Gaussian random field with the linear CDM power spectrum taken from the fitting formulae presented by Eisenstein & Hu (1999). The simulation is performed in a periodic box of side length of $25\ h^{-1}$ Mpc with a 192^3 grid and an equal number of dark matter particles. The universe is evolved from $z = 49$ to 0. The initial temperature is set to $T = 10^4$ K, and the polytropic index takes the value $\gamma = 5/3$. For comparison, two sets of simulations have been performed by using the WENO-E and WENO-S schemes, which update the energy and entropy, respectively, outside the shocked regions (see § 3.3).

Figure 8 plots density contours for the baryonic matter (*bottom panel*) and the cold dark matter (*top panel*) in a slice with two-cell thickness of $0.26\ h^{-1}$ Mpc at $z = 1.5$. In Figure 9 we compare the cell temperature contours drawn from the simulations using the WENO-E (*bottom panel*) and WENO-S (*top panel*) codes. Obviously, the two simulations coincide in the high-temperature ($>10^4$ K) regions, but in the low-temperature regions, the WENO-E simulation gives less fractions of the volume than those from WENO-S. This phenomenon is due to the artificial numerical errors, which heat up significantly the regions with temperature $\leq 10^2$ K to $T \sim 10^2$–10^4 K in the WENO-E calculation. In contrast, since the entropy equation is capable of tracking the temperature field with high accuracy and hence the spurious heating is minimized, the cold unshocked regions occupy more volumes in the WENO-S calculation.

Figure 10 gives an example of density, velocity, and temperature distributions along randomly chosen lines of sight. To
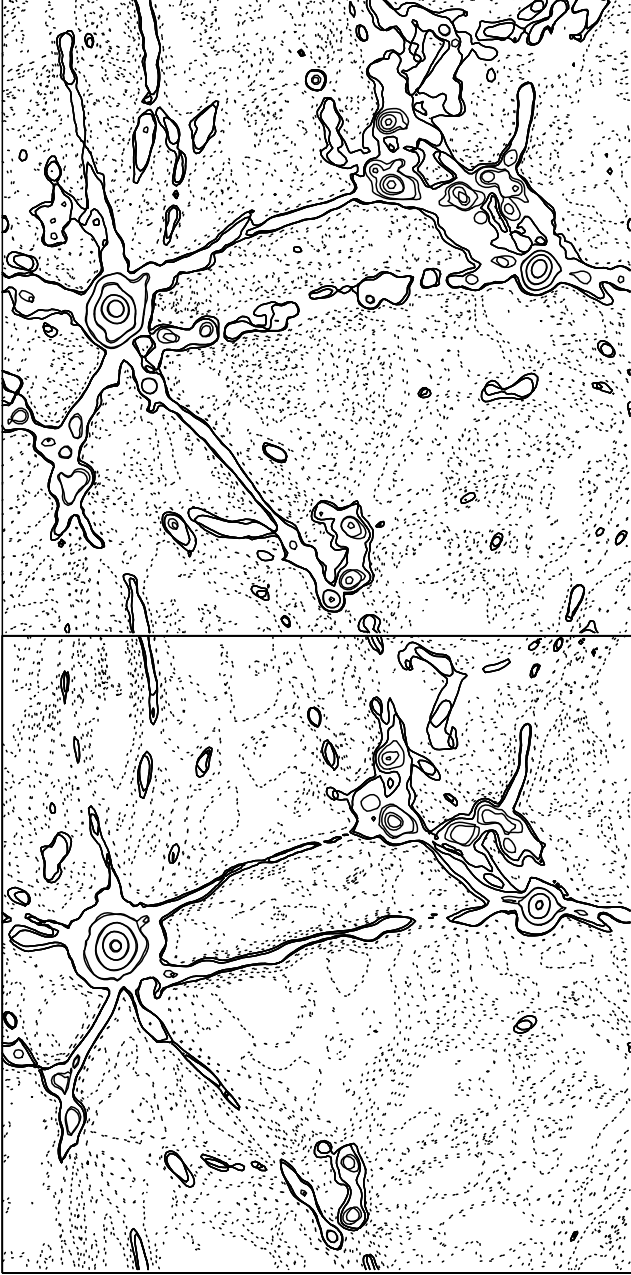
Fig. 8.—Gas density (*bottom panel*) and CDM density (*top panel*) contour plots for a slice of 0.26 h^{-1} Mpc thickness in a 192^3 grid at $z = 1.5$. The solid contours represent overdense regions with $\rho/\bar{\rho} \geq 1$, and the dotted contours represent underdense regions with $\rho/\bar{\rho} \leq 1$.

Fig. 9.—Comparison of temperature contours for the WENO-E (*bottom panel*) and WENO-S (*top panel*) for a slice of 0.26 h^{-1} Mpc thickness in a 192^3 grid at $z = 1.5$. The solid contours represent hot regions with $T \geq 10^4$ K, and the dotted contours represent cold regions with $T < 10^4$ K.

demonstrate further the difference between the WENO-E and WENO-S codes, we plot the results from both calculations in each panel. Once again, the numerical heating in the preshock or unshocked regions is clearly seen in this plot. Our result is compatible with that of Ryu et al. (1993) for a purely baryonic universe. Moreover, it is also noted from Figure 10 that there are not significant differences between the density and velocity fields in the WENO-S and WENO-E calculations, while for the temperature distribution, the difference occurs in the regions of cold gas, $T \leq 10^4$ K. This demonstrates that the internal energy corrections made in cold regions (mostly in unshocked gas) by the modified entropy equation have little dynamical effect on the flow structure except for the internal energy or temperature fields.
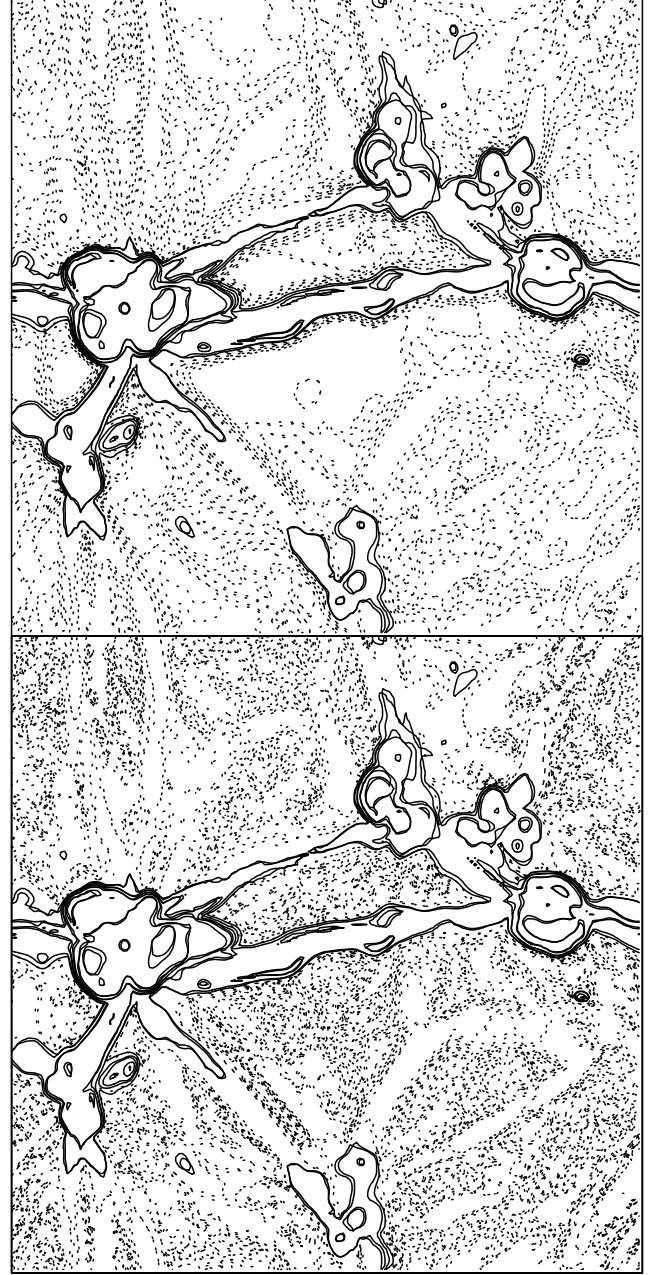
In Figure 11 we present an alternative view of the difference between the WENO-E and WENO-S codes by plotting histograms of the volume-weighted (*top panel*) and mass-weighted (*bottom panel*) temperature on the 192^3 grids. Clearly, the artificial numerical heating is serious in the regions occupied by the low-temperature gas in the WENO-E calculation; however, it is less significant in the fraction of mass. Another illustration indicating such a difference can be given by contour plots of the volume fraction with given temperature and density. As displayed in Figure 12, the volume difference only occurs in the low-density/low-temperature regions with $\rho/\bar{\rho} \leq 1$ and $T \leq 10^4$ K, typically around $\rho/\bar{\rho} \sim 0.1$, $T \sim 10^3$ K. It should be noted that although the spurious heating does exist also in the standard WENO code, it is weaker than those in
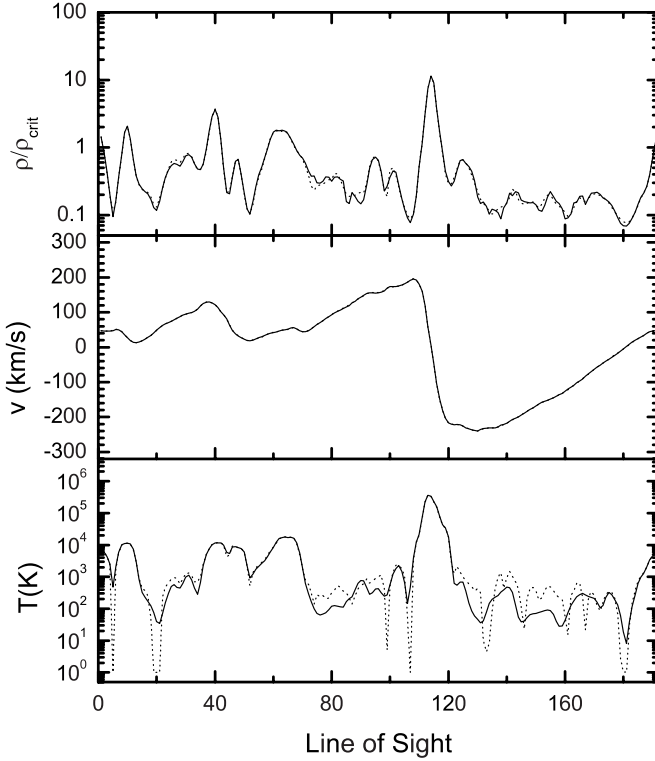
Fig. 10.—Density, velocity, and temperature distributions along randomly chosen lines of sight at $z = 1.5$. The solid lines are for the WENO-S simulation, and the dotted lines are for the WENO-E simulation.

low-order schemes, e.g., the second-order TVD code of Ryu et al. (1993). This benefit clearly comes from the higher order accuracy acquired in our fifth-order WENO scheme, which leads to smaller numerical errors in the calculations. However, for realistic cosmological simulations, such a difference may not be significant while the radiation field is taken into account. For instance, in the presence of ionizing UV background, the baryonic intergalactic medium could be heated up to $\sim 10^4$ K. The simulation including the radiative heating-cooling and ionization and relevant statistical analysis will be presented elsewhere.

5. CONCLUDING REMARKS

In this paper we have described a newly developed hybrid cosmological hydrodynamic code based on weighted essentially nonoscillatory (WENO) schemes for the Euler system of conservation laws. We implement the fifth-order finite-difference WENO to solve the inviscid fluid dynamics on a uniform Eulerian grid combined with a third-order low-storage Runge-Kutta TVD scheme for advancing in time. In order to solve the cosmological problem involving both collisional baryonic matter and collisionless dark matter, we incorporate the particle-mesh method for computing the self-gravity into our cosmological code.

The code has been subjected to a number of tests for accuracy and convergence. As expected, the WENO scheme demonstrates its capacity of capturing shocks and producing sharp and nonoscillatory discontinuity transition without generating oscillations. In comparison with other existing hydrodynamic codes such as the TVD or PPM schemes, one striking feature of the WENO code is that it retains higher order accuracy in smooth regions including at smooth extrema even in multidimensions, and yet it is still highly stable and robust for strong shocks. In performance, the WENO scheme needs more
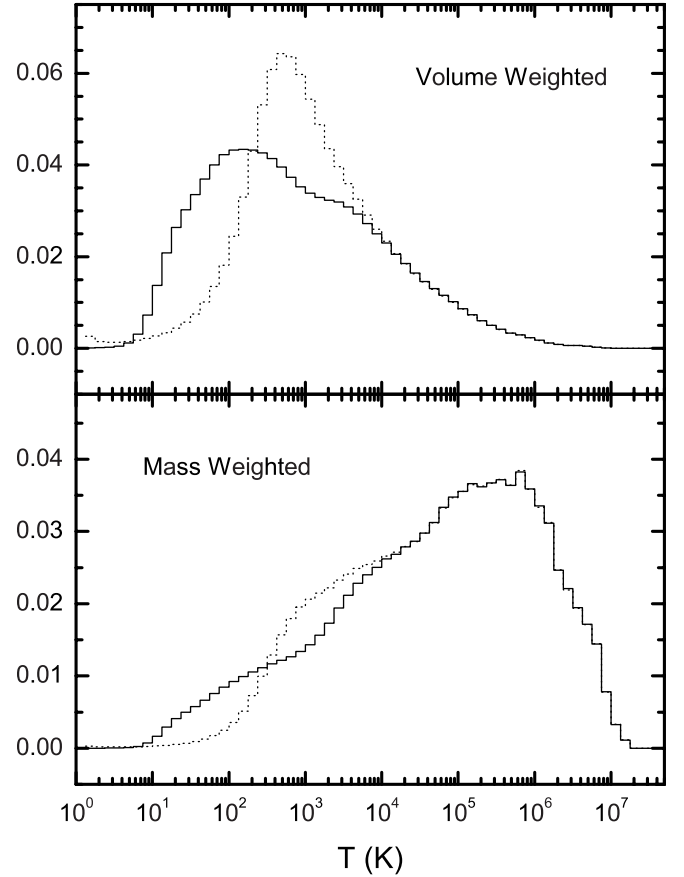

Fig. 11.—Cell temperature histogram in a 192^3 grid at $z = 1.5$. *Top*: Volume-weighted cell temperature; *bottom*: mass-weighted cell temperature. In both panels, the solid lines are for the WENO-S simulation, and the dotted lines are for the WENO-E simulation.

floating point operations per cell than those of the PPM and TVD schemes. However, in compensating for twice or more loss of the computational speed, the WENO scheme achieves both higher order accuracy and convergence rate than PPM and TVD codes according to our numerical tests.

In the presence of gravity, the hydrodynamics becomes more challenging than that without gravity because of the high nonlinearity of gravitational clustering. One serious problem encountered in many cosmological applications is the so-called high Mach number problem. To address this problem, we have incorporated an extra technique into our cosmological
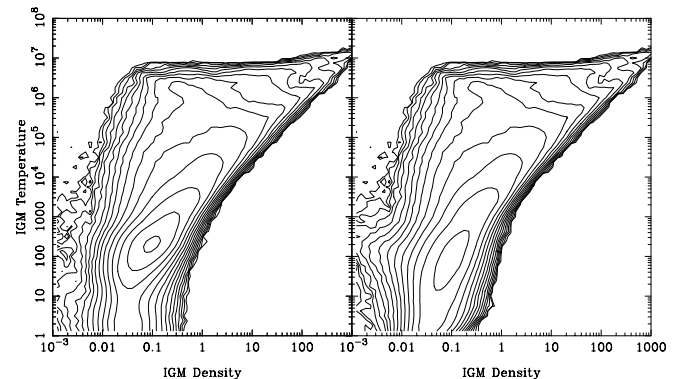

Fig. 12.—Contour plot of the volume with given temperature and density at $z = 1.5$. *Left*: Calculation with the WENO-E; *right*: calculation with the WENO-S.

WENO/PM code, which is actually a combination of the dual energy algorithm (Bryan et al. 1995) and the energy-entropy algorithm (Ryu et al. 1993). Namely, instead of solving the internal energy equation in regions free of shocks as was done in the dual energy algorithm (Bryan et al. 1995), we solve the modified entropy equation (Ryu et al. 1993), which takes a conservative form and can be easily solved using the standard WENO scheme. This improvement over our hydrodynamic WENO code ensures an accurate tracking of the temperature field in regions free of shocks.

We point out that the high-order WENO discretization, e.g., the fifth-order WENO scheme adopted in this paper, introduces a quite small numerical viscosity, which does not lead to a significant violation of energy conservation in the presence of gravitational fields, while for a second-order TVD scheme the numerical diffusion is no longer negligible. In order to have a better conservation of the total energy, it is usually corrected by adding a compensation term in the gravitational force term (Ryu et al. 1993).

The Euler hydrodynamics on fixed meshes has several distinct advantages, which include simplicity for implementation, easy data parallelization, relatively low floating point cost, large dynamic range in mass, and high resolution of shock capturing. In particular, the WENO scheme can also achieve a higher accuracy on coarse meshes and a better resolution on the largest meshes allowed by available memory. To be suitable for large simulations of the cosmological problem, further improvement of the hydrodynamic WENO code is needed in its implementation on distributed-memory computers. The parallel version of the code based on the Message Passing Interface (MPI) is under development.

APPENDIX

LOW-STORAGE RUNGE-KUTTA SCHEME

General low-storage Runge-Kutta schemes can be written in the form

$$
\begin{aligned}
du^{(i)} &= A_i\, du^{(i-1)} + \Delta t L\Big(u^{(i-1)},\ t^n + \alpha_i \Delta t\Big), \\
u^{(i)} &= u^{(i-1)} + B_i\, du^{(i)}, \qquad i = 1,\dots,m, \\
u^{(0)} &= u^n, \qquad u^{(m)} = u^{n+1}, \qquad A_1 = 0.
\end{aligned}
\tag{A1}
$$

Only u and du must be stored, resulting in two storage units for each variable, instead of three storage units for equation (8). The third-order nonlinearly stable version we use, Gottlieb & Shu (1998), has $m = 3$ in equation (A1), with

$$
\begin{aligned}
z_1 &= \sqrt{36c_2^4 + 36c_2^3 - 135c_2^2 + 84c_2 - 12}, \\
z_2 &= 2c_2^2 + c_2 - 2, \\
z_3 &= 12c_2^4 - 18c_2^3 + 18c_2^2 - 11c_2 + 2, \\
z_4 &= 36c_2^4 - 36c_2^3 + 13c_2^2 - 8c_2 + 4, \\
z_5 &= 69c_2^3 - 62c_2^2 + 28c_2 - 8, \\
z_6 &= 34c_2^4 - 46c_2^3 + 34c_2^2 - 13c_2 + 2, \\
B_1 &= c_2, \\
B_2 &= \frac{12c_2(c_2 - 1)(3z_2 - z_1) - (3z_2 - z_1)^2}{144c_2(3c_2 - 2)(c_2 - 1)^2}, \\
B_3 &= \frac{-24(3c_2 - 2)(c_2 - 1)^2}{(3z_2 - z_1)^2 - 12c_2(c_2 - 1)(3z_2 - z_1)}, \\
A_2 &= \frac{-z_1\big(6c_2^2 - 4c_2 + 1\big) + 3z_3}{(2c_2 + 1)z_1 - 3(c_2 + 2)(2c_2 - 1)^2}, \\
A_3 &= \frac{-z_4 z_1 + 108(2c_2 - 1)c_2^5 - 3(2c_2 - 1)z_5}{24z_1 c_2(c_2 - 1)^4 + 72c_2 z_6 + 72c_2^6(2c_2 - 13)}, \\
\alpha_1 &= 0, \\
\alpha_2 &= B_1, \\
\alpha_3 &= B_1 + B_2(A_2 + 1),
\end{aligned}
\tag{A2}
$$

where $c_2 = 0.924574$.

REFERENCES

Balsara, D., & Shu, C.-W. 2000, J. Comput. Phys., 160, 405
Bertschinger, E. 1998, ARA&A, 36, 599
Bryan, G. L., Norman, M. L., Stone, J. M., Cen, R., & Ostriker, J. P. 1995, Comput. Phys. Commun., 89, 149
Cen, R. 1992, ApJS, 78, 341
Colella, P., & Woodward, P. R. 1984, J. Comput. Phys., 54, 174
Couchman, H. M. P., Thomas, P. A., & Pearce, F. R. 1995, ApJ, 452, 797
Del Zanna, L., Velli, M., & Londrillo, P. 1998, A&A, 330, L13
Efstathiou, G., Davis, M., Frenk, C. S., & White, S. D. M. 1985, ApJS, 57, 241
Eisenstein, D. J., & Hu, W. 1999, ApJ, 511, 5
Evrard, A. E. 1988, MNRAS, 235, 911
Giacconi, P., Gursky, H., Paolini, F., & Rossi, B. 1962, Phys. Rev. Lett., 9, 439
Gingold, R. A., & Monaghan, J. J. 1977, MNRAS, 181, 375
Gnedin, N. Y. 1995, ApJS, 97, 231
Gottlieb, S., & Shu, C.-W. 1998, Math. Comput., 67, 73
Gottlieb, S., Shu, C.-W., & Tadmor, E. 2001, SIAM Rev., 43, 89
Grasso, F., & Pirozzoli, S. 2000a, Phys. Fluids, 12, 205
———. 2000b, Theor. Comput. Fluid Dyn., 13, 421
Harten, A. 1983, J. Comput. Phys., 49, 357
Harten, A., Engquist, B., Osher, S. J., & Chakravarthy, S. 1987, J. Comput. Phys., 71, 231
Hernquist, L., & Katz, N. 1989, ApJS, 70, 419
Hockney, R. W., & Eastwood, J. W. 1988, Computer Simulation Using Particles (Philadelphia: IOP)
Jiang, G., & Peng, D. P. 2000, SIAM J. Sci. Stat. Comput., 21, 2126
Jiang, G., & Shu, C.-W. 1996, J. Comput. Phys., 126, 202
Jiang, G., & Wu, C.-C. 1999, J. Comput. Phys., 150, 561
Landau, L. D., & Lifshitz, E. M. 1987, Fluid Mechanics (2nd ed.; Oxford: Pergamon Press)
Liang, S., & Chen, H. 1999, AIAA J., 37, 1010
Liska, R., & Wendroff, B. 1998, SIAM J. Numer. Anal., 35, 2250
———. 1999, Int. J. Numer. Meth. Fl., 30, 461
Liu, X. D., Osher, S. J., & Chan, T. 1994, J. Comput. Phys., 115, 200
Lucy, L. B. 1977, AJ, 82, 1013
Montarnal, P., & Shu, C.-W. 1999, J. Comput. Phys., 148, 59
Mulchaey, J. S. 2000, ARA&A, 38, 289
Navarro, J. F., & White, S. D. M. 1993, MNRAS, 265, 271
Noelle, S. 2000, J. Comput. Phys., 164, 283

Norman, M. L., & Bryan, G. L. 1999, in Numerical Astrophysics 1998, ed. S. Miyama, K. Tomisaka, & T. Hanawa (Boston: Kluwer), 19
O'Shea, B. W., Bryan, G., Bordner, J., Norman, M. L., Abel, T., Harkness, R., & Kritsuk, A. 2004, in Adaptive Mesh Refinement—Theory and Applications, ed. T. Plewa, T. Linde, & V. G. Weirs (Berlin: Springer), in press
Ostriker, J. P., & Vishniac, E. T. 1986, ApJ, 306, L51
Owen, J. M., Villumsen, J. V., Shapiro, P. R., & Martel, H. 1998, ApJS, 116, 155
Pen, U. L. 1998, ApJS, 115, 19
Rauch, M. 1998, ARA&A, 36, 267
Ricker, P. M., Dodelson, S., & Lamb, D. Q. 2000, ApJ, 536, 122
Roe, P. 1978, J. Comput. Phys., 27, 1
Ryu, D., Ostriker, J. P., Kang, H., & Cen, R. 1993, ApJ, 414, 1
Sedov, L. I. 1993, Similarity and Dimensional Methods in Mechanics (10th ed.; Boca Raton: CRC)
Shi, J., Zhang, Y. T., & Shu, C.-W. 2003, J. Comput. Phys., 186, 690
Shu, C.-W. 1988, SIAM J. Sci. Stat. Comput., 9, 1073
———. 1998, in Advanced Numerical Approximation of Nonlinear Hyperbolic Equations, ed. B. Cockburn, C. Johnson, C.-W. Shu, & E. Tadmor (Berlin: Springer), 325
———. 1999, in High-Order Methods for Computational Physics, ed. T. J. Barth & H. Deconinck (Berlin: Springer), 439
———. 2003, Int. J. Comput. Fluid Dyn., 17, 107
Shu, C.-W., & Osher, S. J. 1988, J. Comput. Phys., 77, 439
Sod, G. A. 1978, J. Comput. Phys., 27, 1
Sornborger, A., Fryxell, B., Olson, K., & MacNeice, P. 1996, preprint (astro-ph/9608019)
Springel, V., Yoshida, N., & White, S. D. M. 2001, NewA, 6, 79
Steinmetz, M. 1996, MNRAS, 278, 1005
Stone, J. M., & Norman, M. L. 1992, ApJS, 80, 753
Teyssier, R. 2002, A&A, 385, 337
Turner, M. S. 2002, ApJ, 576, L101
Walker, T., Steigma, G., Schramm, D. N., Olive, K. A., & Kang, H. S. 1991, ApJ, 376, 51
Yang, J., Yang, S., Chen, Y., & Hsu, C. 1998, J. Comput. Phys., 146, 464
Zel'dovich, Ya. B. 1970, A&A, 5, 84
Zel'dovich, Ya. B., & Sunyaev, R. A. 1969, Ap&SS, 4, 301